A High-Resolution Airborne SAR Autofocusing Approach Based on SR-PGA and Subimage Resampling With Precise Hyperbolic Model

Yuhui Deng, *Graduate Student Member, IEEE*, Hui Wang, *Senior Member, IEEE*, Guang-Cai Sun, *Senior Member, IEEE*, Yong Wang, *Senior Member, IEEE*, Wenkang Liu, *Member, IEEE*, Jun Yang, *Member, IEEE*, and Mengdao Xing, *Fellow, IEEE*

***Abstract*—High-resolution airborne synthetic aperture radar imaging requires long synthetic aperture time (LSAT). However, the LSAT invalidates the Fresnel approximation in the traditional autofocusing method, leaving a residual signal phase in the motion error. To solve the problem, a signal-reconstruction-based phase gradient autofocus (SR-PGA) and a subimage resampling (SIR) methods are proposed. They are developed on the hyperbolic model. First, a subaperture division strategy divides the full-aperture high-order error into multiple low-order subaperture errors (SPEs). Then, the SR-PGA is developed to estimate the SPE, in which the precise deramping is reconstructed to eliminate the residual signal phase in the SPE. Third, the SIR is proposed to eliminate residual Doppler-variant shift of the adjacent subimages, improving the accuracy of the SPE combination. Finally, simulation and actual data processing verify the effectiveness and validity of the algorithm.**

***Index Terms*—Doppler subimage resampling, hyperbolic model, long synthetic aperture, SAR autofocusing, signal-reconstruction-based phase gradient autofocus (SR-PGA), synthetic aperture radar (SAR).**

I. Introduction

DUE to atmospheric disturbance or pilot error, the actual motion trajectory of an airborne synthetic aperture radar (SAR) may easily deviate from a straight line, and the acquired raw data cannot be directly focused due to the existence of motion errors [1], [2], [3], [4], [5], [6]. Such motion errors can be compensated by measuring the deviations, through the inertial navigation system (INS) and global positioning system (GPS) unit. However, these measurements are required to reach a precision of subwavelength scale to obtain high-resolution SAR images [5], [7]. Autofocus methods are usually employed to estimate motion error from the acquired radar data beyond the accuracy of the motion-measurement instrumentations [5], [8], [9], [10]. Thus, it is necessary to estimate and correct the motion errors using autofocus methods accurately from the acquired radar data [11], [12], [13].

Motion errors usually consist of an envelope error and a phase one, and both types of errors satisfy the linear mapping relationship, that is, the ratio of the phase error to the envelope error is $4\pi/\lambda$. Some researchers calculate the phase error by estimating the envelope error [14], [15], [16], but others convert the phase error estimated by phase autofocusing methods into the envelope error [2], [6], [17], [18]. In the first-class methods, the cross-correlation method based on oversampled data of range profiles is employed to estimate the envelope error. However, the accuracy of the error estimation only reaches the envelope scale and cannot meet the imaging requirements. Therefore, the phase error estimation methods, whether parametric or nonparametric ones, are commonly used. In the former ones, a polynomial phase error model is established after the model parameterization. The map drift (MD) technique is the common and robust approach [2], [19]. It assumes the phase error is quadratic and estimates the quadratic coefficients of the phase error through the correlation processing of two adjacent subimages. The latter ones typically extract the phase or phase gradient of the motion error from the raw data directly, and among which, the phase gradient autofocus (PGA) method and its extended algorithms (e.g., [8], [9], [18], [20], [21], [22]) are representative and widely used.

The original PGA is suitable for the spotlight mode and the motion errors of scatterers in the processed scene are consistent. In this case, a full-aperture phase error can be directly estimated by PGA. However, for the stripmap mode, the scene illuminated by the radar changes with the movement of the aircraft, and

Manuscript received 20 September 2022; revised 3 November 2022 and 15 December 2022; accepted 17 January 2023. Date of publication 31 January 2023; date of current version 2 March 2023. This work was supported in part by the Fundamental Research Funds for the Central Universities under Grant ZDRC2201; in part by the National Natural Science Foundation of China under Grant 62101404, Grant 61931025, and Grant 62222113; in part by the National Science Fund for Distinguished Young Scholars under Grant 61825105; and in part by the Shanghai Aerospace Science and Technology Innovation Fund. *(Corresponding authors: Hui Wang; Wenkang Liu.)*

Yuhui Deng and Guang-Cai Sun are with the National Laboratory of Radar Signal Processing, Xidian University, Xi'an 710071, China (e-mail: dengyuhui2018@163.com; rsandsgc@126.com).

Hui Wang is with the Key Laboratory of Millimeter Wave Imaging Technology, Shanghai Institute of Satellites Engineering, Shanghai 201100, China (e-mail: huiwang@mml-ciss.org).

Yong Wang is with the School of Resources and Environment, University of Electronic Science and Technology of China, Chengdu 611731, China (e-mail: wangy@ecu.edu).

Wenkang Liu is with the Academy of Advanced Interdisciplinary Research, Xidian University, Xi'an 710071, China (e-mail: wkliu@stu.xidian.edu.cn).

Jun Yang is with the College of Geomatics, Xi'an University of Science and Technology, Xi'an 710071, China (e-mail: yangjun_kx@163.com).

Mengdao Xing is with the National Laboratory of Radar Signal Processing and the Academy of Advanced Interdisciplinary Research, Xidian University, Xi'an 710071, China (e-mail: xmd@xidian.edu.cn).

Digital Object Identifier 10.1109/JSTARS.2023.3241169

the motion error of scatterers varies with the different scenes. Therefore, PGA cannot be directly employed in stripmap long synthetic aperture processing [8]. Fortunately, the subaperture (SA) division can be employed to solve this problem. In the SA, it can be seen as a spotlight mode for an SA and PGA can be employed. However, another problem arises. With the increase of synthetic aperture interval, the number of SA becomes larger and the subaperture error (SPE) combination should be considered to obtain the full-aperture phase error.

Many scholars have done a lot of work on SA processing. Liu et al. [23] use the SA image coherent superposition to achieve high-resolution real-time imaging for spotlight SAR. Estimate the azimuth SA envelope and phase errors by the cross-correlation-based algorithm and map-drift method in the range-Doppler domain. Hai et al. [24] propose an optimal SA division method to guarantee the coherence of each SA data in the back-projection imaging. Yan et al. [25] achieve the along-track motion compensation based on the SA processing. Prats et al. [26] use SAs in the time domain to accommodate accurate topography and compensate for azimuth coregistration errors. Potsis et al. [27] propose an SA approach for residual motion compensation in azimuth processing. Bezvesilniy et al. [29] estimate and integrate the local quadratic phase error in the SA to obtain the full-aperture phase error.

For high-resolution airborne SAR imaging, the synthetic aperture interval is long and it is essential to estimate the full-aperture phase error accurately [6]. Therefore, the SA processing is used to estimate the full-aperture motion errors. As mentioned earlier, the accuracy of the SPE estimation and the SPE combination determines the accuracy of the full-aperture error estimation.

For the SPE estimation, Ding et al. [18] use the resampling weight PGA to estimate the SPEs in the SA back-projection imageries. Chen et al. [3] combine PGA and the weighted least square method to improve the robustness of PGA. Mao et al. [12] propose a knowledge-aided 2-D autofocus method using PGA, in which PGA is employed to estimate the azimuth-frequency phase error. Meanwhile, the SPE combination is employed to obtain the full-aperture motion errors. Thompson et al. [29] combine the SPEs after eliminating the mean difference between the SPEs' gradient obtained from the overlapped samples of the adjacent SAs. Zhu et al. [30] study a multi-subaperture PGA approach to obtain the full-aperture phase error, taking advantage of the Fresnel approximation.

However, in the aforementioned algorithms, the Fresnel approximation is employed in the SPE estimation and the SPE combination. In the SPE estimation, the Fresnel approximation used in PGA causes the residual signal phase. In addition, the Fresnel approximation introduces the residual Doppler-variant shift in the SPE combination, which decreases the estimation accuracy of the full-aperture phase error.

For the aforementioned problems in the SPE estimation and the SPE combination, an airborne SAR autofocusing approach based on the signal-reconstruction-based PGA (SR-PGA) and subimage resampling methods is proposed by introducing the precise hyperbolic model. The SR-PGA is proposed to precisely estimate the SPE, in which the precise deramping is reconstructed with the hyperbolic mode and the Doppler information

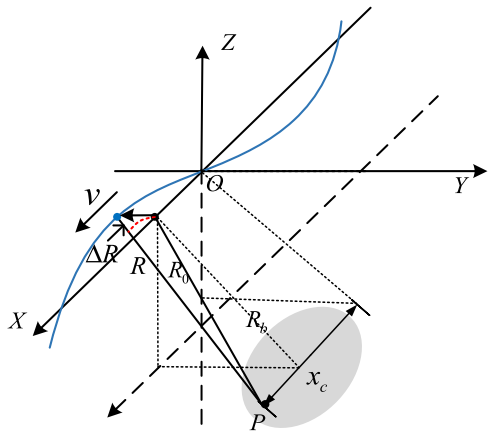

Fig. 1. Airborne SAR imaging geometry with motion errors.

TABLE I
SYSTEM PARAMETERS IN SIMULATION

Parameters	Value
Central frequency	9.63 GHz
Signal bandwidth	1.3 GHz
Center slant range	8600 m
Platform velocity	110 m/s
Pulse repetition frequency	2000 Hz

of the main lobe center. The residual signal phase is eliminated by precise deramping. After the precise deramping, we can obtain subimages in the range-time and azimuth-frequency domains. The SIR method is proposed to resample the subimage in the Doppler domain. According to the method, the residual Doppler-variant shift of the adjacent subimages caused by the signal is directly eliminated, and the real shift caused by the linear motion error can be precisely estimated. Therefore, the method improves the combination accuracy of the SPEs. Then, the full-aperture phase error is adequately obtained with the SPE combination. Finally, the residual RCM and phase error in the raw data are compensated for, and a well-focused airborne SAR image is obtained.

This article is organized as follows. In Section II, the motion errors in an SA are analyzed. The algorithm is detailed in Section III. In Section IV, the algorithm is validated with acquired SAR data. The applicability of the algorithm is discussed in Section V. Finally, Section VI concludes this article.

II. Analysis of Motion Errors in a Subaperture

A. Signal Model in Subaperture

Fig. 1 shows the SAR geometric model with motion errors. The *X*-axis denotes a straight and ideal trajectory in data acquisition. The antenna phase center of airborne SAR moves along the nominal trajectory with a constant velocity v. The blue curve is the actual flight path. P is a point target located within an observed ground scene. R is the instantaneous slant range from SAR to P. R_b denotes the nearest slant range between the trajectory and P, and O is the central moment of azimuth time. x_c is the azimuth distance between O and P. After the initial

MOCO using the INS and GPS data, the slant range of P as a function of full-aperture azimuth time t_a can be written as

$$R(t_a, R_b) = R_0(t_a, R_b) + \Delta R(t_a, R_b) \tag{1}$$

where $t_a \in (-n_a/2, n_a/2-1)/PRF$, n_a is the full-aperture azimuth sample number, n_r is the range sample number, F_s is the range sampling rate, and the instantaneous slant range on the straight trajectory $R_0(t_a, R_b) = \sqrt{R_b^2 + (vt_a - x_c)^2}$. $\Delta R(t_a, R_b)$ represents the slant range error caused by motion errors. The transmitted waveform is assumed to be

$$s_t(t_r) = \text{rect}\left(\frac{t_r}{T_p}\right)\exp\left(j\pi\left(\gamma_r t_r^2 + 2f_c t_r\right)\right) \tag{2}$$

where $\text{rect}(\cdot)$ represents the range modulation. The range fast-time $t_r \in (-n_r/2, n_r/2-1)/F_s$, T_p is the pulsewidth, γ_r is the chirp rate, and f_c is the central frequency.

With P as an example, the received range time-domain signal, after modulating to the baseband, is

$$\begin{aligned} s_r(t_a, t_r, R_b) &= \text{rect}\left(\left(t_r - \tfrac{2R(t_a,R_b)}{c}\right)\Big/T_p\right) W_a(t_a) \\ &\times \exp\left(j\left(\gamma_r \pi\left(t_r - \tfrac{2R(t_a,R_b)}{c}\right)^2 - \tfrac{4\pi R(t_a,R_b)}{\lambda}\right)\right) \end{aligned} \tag{3}$$

where $W_a(\cdot)$ is the azimuth amplitude modulation. c is the speed of light and the radar wavelength. After using an SAR imaging algorithm (e.g., extended range migration algorithm (ERMA) [31]) to achieve the range pulse compression and the range cell migration correction (RCMC), one has the 2-D time-domain signal

$$\begin{aligned} s(t_a, t_r, R_b) &= \text{sinc}\left(B_r\left(t_r - \tfrac{2\left(R_b + \Delta r^{SM} + \Delta R(t_a,R_b)\right)}{c}\right)\right) \\ &\times W_a(t_a)\exp\left(-j\tfrac{4\pi}{\lambda}\left(R_0(t_a, R_b) + \Delta R(t_a, R_b)\right)\right) \end{aligned} \tag{4}$$

where B_r is the signal bandwidth, Δr^{SM} is an additional non-system envelope error introduced by the Stolt mapping in the ERMA [8]. For Δr^{SM}, the down-sampling operation in range dimension and the iterative strategy will decrease the effect of the additional envelope errors and frequency domain distortion. The down-sampling operation is achieved by summing up adjacent range cells into one cell or extracting a part of the range frequency band. Fortunately, the Stolt mapping does not change the phase error in the data. Therefore, only the exponential terms of the signal are expressed for the sake of simplicity in the following derivations.

To estimate the motion errors in azimuth, one divides the full-aperture into N overlapped SAs. The SA azimuth sample number is n_a^{SA}, the adjacent SA spacing is $\Delta T = n_a^{ol}/PRF$, and n_a^{ol} is the overlapping sample number of the adjacent SAs. Then, considering P, one analyzes the signal in each SA. The nth SA signal phase of P in the azimuth time domain is defined as

$$\begin{aligned} &s_n(t_{\text{sub}}, R_b) \\ &= \exp\left(-j\tfrac{4\pi}{\lambda}R_{\text{sub}}(t_{\text{sub}}, R_b) + j\varphi_n(t_{\text{sub}}, R_b)\right) \\ &= \exp\left(-j\tfrac{4\pi}{\lambda}\sqrt{R_b^2 + \left(v\left(\Delta t_n + t_{\text{sub}}\right)\right)^2} + j\varphi_n(t_{\text{sub}}, R_b)\right) \\ &\times 1 \le n \le N \end{aligned} \tag{5}$$

where $R_{\text{sub}}(t_{\text{sub}}, R_b)$ is the slant range within the nth SA, the divided SA number is $N = ((n_a - n_a^{SA})/n_a^{ol}) + 1$, and $t_{\text{sub}} \in (-n_a^{SA}/2, n_a^{SA}/2)/PRF$ is the SA azimuth time. t_n is the central time of the nth SA, and $t_c = x_c / v$. Δt_n is the azimuth-time spacing between t_c and t_n. Note that the hyperbolic mode is shown as the first term of the second line in (5). One expands R_{sub} into a Taylor series as

$$R_{\text{sub}}(t_{\text{sub}}, R_b) = \sum_{i=0}^{M}\eta_i(\Delta t_n, R_b)\cdot t_{\text{sub}}^i, M \ge 2 \tag{6}$$

where the zeroth, first, and second components are

$$\eta_0(\Delta t_n, R_b) = \sqrt{R_b^2 + (v\Delta t_n)^2} \tag{7a}$$

$$\eta_1(\Delta t_n, R_b) = \frac{v^2\Delta t_n}{\sqrt{R_b^2 + (v\Delta t_n)^2}}, \text{and} \tag{7b}$$

$$\eta_2(\Delta t_n, R_b) = \frac{v^2 R_b^2}{2\sqrt[3]{R_b^2 + (v\Delta t_n)^2}} \tag{7c}$$

respectively. In addition, the nth SPE in the azimuth time domain is

$$\varphi_n(t_{\text{sub}}, R_b) = -4\pi\Delta R_n(t_{\text{sub}}, R_b)/\lambda \tag{8a}$$

and its expansion as a Taylor series is

$$\varphi_n(t_{\text{sub}}, R_b) = a_n + b_n t_{\text{sub}} + \theta_n(t_{\text{sub}}, R_b) \tag{8b}$$

where a_n is a constant and b_n is a coefficient of the first-order term. $\theta_n(t_{\text{sub}})$ represents all higher order components.

Then, the nth SA signal phase (5) in the azimuth time domain can be rewritten as

$$\begin{aligned} &s_n(t_{\text{sub}}, R_b) = \exp \\ &\times\begin{pmatrix} -j\left(\frac{4\pi}{\lambda}\eta_0(\Delta t_n, R_b) - a_n\right) \\ -j2\pi\left(\frac{2}{\lambda}\eta_1(\Delta t_n, R_b) - \frac{b_n}{2\pi}\right)t_{\text{sub}} \\ -j\left(\frac{4\pi}{\lambda}\sum_{i=2}^{M}\eta_i(\Delta t_n, R_b)\cdot t_{\text{sub}}^i - \theta_n(t_{\text{sub}}, R_b)\right) \end{pmatrix}. \end{aligned} \tag{9}$$

After applying a Fourier transform (FT) to (9) in the azimuth-time domain, the transformed signal in the range-Doppler domain is expressed as

$$\begin{aligned} &S_n(f_a, R_b) = \exp\left(-j\left(\tfrac{4\pi}{\lambda}\eta_0(\Delta t_n, R_b) - a_n\right)\right) \\ &\cdot\text{sinc}\left(T_{\text{sub}}\left(f_a - \left(\tfrac{2}{\lambda}\eta_1(\Delta t_n, R_b) - \tfrac{b_n}{2\pi}\right)\right)\right) \\ &\otimes\Omega(f_a, R_b)\otimes E(f_a, R_b), 1 \le n \le N \end{aligned} \tag{10}$$

where $\otimes$ denotes the convolution operation, and the azimuth frequency $f_a \in (-n_a^{SA}/2, n_a^{SA}/2-1)/n_a^{SA}\cdot PRF$. The first term has a constant phase, which does not affect the SA imaging focus. The second one is the azimuth-compressed expression

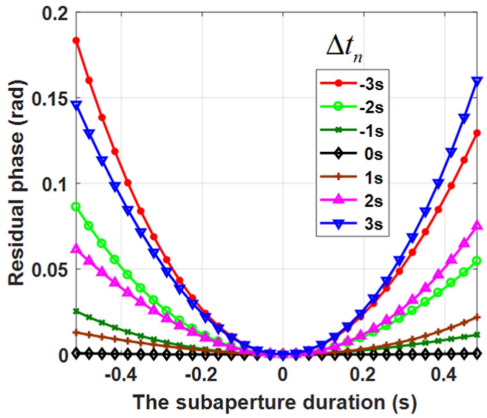

Fig. 2. Residual as a function of Δt_n.

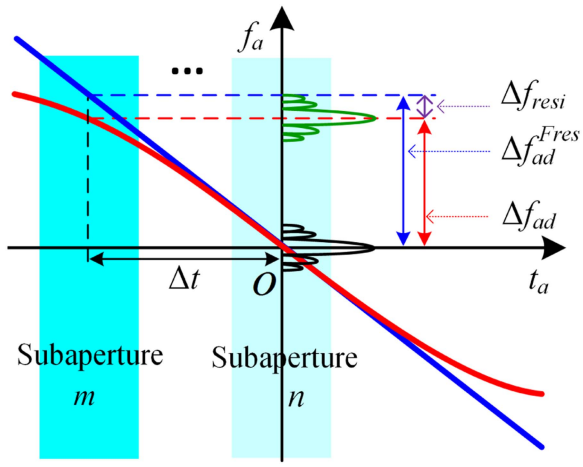

Fig. 3. Doppler shifts of the same scatterer between the adjacent SA images.

of the SA data in the range-Doppler domain. $\Omega(f_a, R_b)$ is the FT result of $\exp(-j\frac{4\pi}{\lambda}\sum_{i=2}^{M}\eta_i(\Delta t_n, R_b)\cdot t_{\text{sub}}^i)$. $E(f_a, R_b)$ is $\exp(j\theta_n(t_{\text{sub}}, R_b))$ after the FT. $\Omega(f_a, R_b)$ and $E(f_a, R_b)$ defocuses the azimuth-compressed SA image. To obtain the full-aperture phase error precisely, one should estimate b_n and $\theta_n(t_{\text{sub}}, R_b)$ in each SA.

B. Analysis of Residual Signal Phase Caused by Fresnel Approximation

The azimuth time-domain SA signal phase history in the first term of (5) is hyperbolic and relates to the azimuth time spacing Δt_n. Note that Δt_n increases as beamwidth increases. Unlike the hyperbolic model, the Fresnel approximation considers that the signal history is quadratic. According to the Fresnel approximation, one removes the quadratic signal phase by a deramping function in PGA before estimating the SPE in the azimuth time domain. The function is

$$s_{de}\left(t_{\text{sub}}, R_b\right) = \exp\left(j\pi\gamma t_{\text{sub}}^2\right) \tag{11}$$

with $\gamma = 2v^2/(\lambda R_b)$. A residual signal phase of the nth SA in the azimuth time domain can be expressed as

$$\phi_{\text{resi}}\left(t_{\text{sub}}, R_b\right) = \exp\left(-j\frac{4\pi}{\lambda}\sum_{i=2}^{M}\eta_i\left(\Delta t_n, R_b\right)\cdot t_{\text{sub}}^i + j\pi\gamma t_{\text{sub}}^2\right) \tag{12}$$

To understand the residual signal phase $\phi_{\text{resi}}(t_{\text{sub}}, R_b)$, we simulated with the main parameters given in Table I. The results are shown in Fig. 2. The larger $|\Delta t_n|$ is, the larger the residual phase. Thus, $\phi_{\text{resi}}(t_{\text{sub}}, R_b)$ caused by the Fresnel approximation can significantly affect the accuracy of the SPE estimation.

C. Analysis of Residual Doppler-Variant Doppler Shift Caused by Fresnel Approximation

After obtaining the multiple SPEs, one should estimate the linear error in each SA to achieve the SPE combination, and one can obtain the linear error by estimating b_n in the nth SA. According to (10), it can be known that a coefficient b_n of the first-order error shifts the Doppler SA image. Thus, b_n can be

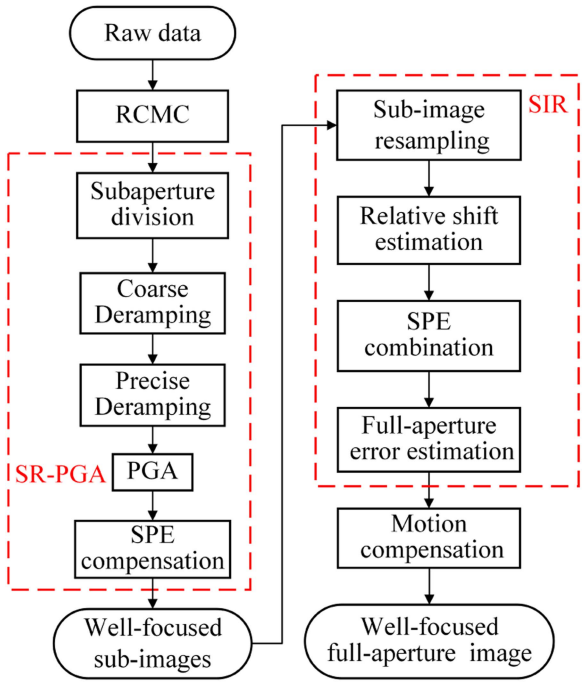

Fig. 4. Flowchart of the proposed algorithm.

estimated by evaluating the Doppler shift between the adjacent SA images [9], [30].

With (7b) and the second term in (10), the focused Doppler frequency position of P in the nth SA image in the range-Doppler domain is

$$f_n = \frac{2}{\lambda}\frac{v^2\Delta t_n}{\sqrt{R_b^2 + (v\Delta t_n)^2}} - \frac{b_n}{2\pi}. \tag{13}$$

Similarly, the focused position of P in the mth SA image in the range-Doppler domain can be expressed as

$$f_m = \frac{2}{\lambda}\frac{v^2\Delta t_m}{\sqrt{R_b^2 + (v\Delta t_m)^2}} - \frac{b_m}{2\pi} \tag{14}$$

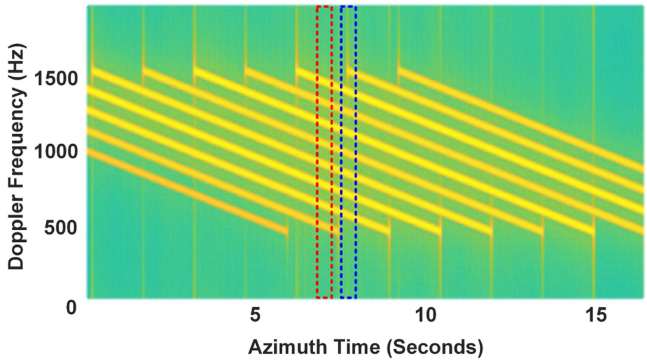

Fig. 5. Diagram of a line signal consisting of signals of eight-point targets.

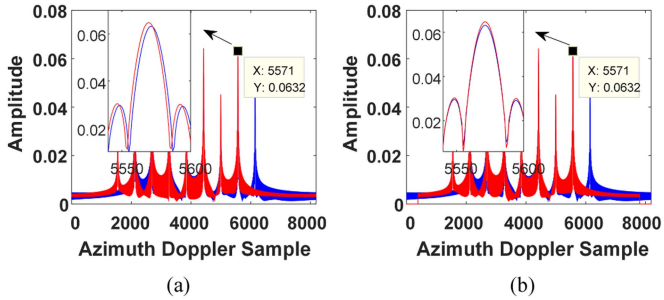

Fig. 6. SA image alignment results based on the (a) Fresnel approximation and the (b) SIR method.

where $\Delta t_m = \Delta t_n + \Delta t$. The azimuth time interval Δt is $(m-n)T_{\text{sub}}$, and T_{sub} is the azimuth duration of each SA. Then, the Doppler shift between the nth and mth SA images in the range-Doppler domain is

$$\Delta f_{mn} = |f_m - f_n| = |\Delta f_{ad}| + \frac{1}{2\pi}|b_n - b_m|. \tag{15}$$

In (15), $\frac{1}{2\pi}|b_n - b_m|$ is the relative Doppler shift between the nth and mth SA images caused by the linear phase error, and it can be used to estimate the linear phase error in the azimuth time domain. And there is an inherent Doppler-variant Doppler shift of the adjacent SA images Δf_{ad} or

$$\Delta f_{ad} = \left| \frac{2}{\lambda} \frac{v^2 \Delta t_m}{\sqrt{R_b^2 + (v\Delta t_m)^2}} - \frac{2}{\lambda} \frac{v^2 \Delta t_n}{\sqrt{R_b^2 + (v\Delta t_n)^2}} \right|. \tag{16}$$

However, under the Fresnel approximation [30], the inherent Doppler shift Δf_{ad} is replaced by $\Delta f_{ad}^{\text{Fres}}$ or

$$\Delta f_{ad}^{\text{Fres}} = \left| \frac{2v^2}{\lambda R_b} \Delta t \right| \tag{17}$$

and it is Doppler-invariant. Note that there is a residual Doppler-variant Doppler shift between Δf_{ad} and $\Delta f_{ad}^{\text{Fres}}$, and the shift is

$$\Delta f_{\text{resi}} = \left| \Delta f_{ad} - \Delta f_{ad}^{\text{Fres}} \right|. \tag{18}$$

It should be noted that the difference is due to the Fresnel approximation and the difference will cause a biased estimation of b_n.

Fig. 3 demonstrates Δf_{ad}, $\Delta f_{ad}^{\text{Fres}}$, and Δf_{resi} derived from the same scatterer of the adjacent SA images as functions of Δt_n. In the figure, the solid red curve shows the time-frequency line of a real echo signal phase with the hyperbolic form, and the solid blue line represents the time-frequency line with the Fresnel approximation. The two cyan boxes indicate the mth and nth SAs, respectively. After the deramping operation, the focusing positions in the Doppler domain of the same scatterer in the mth and nth SAs are the green and black curves, respectively. Δf_{ad} in Fig. 3 is the inherent Doppler shift of the focusing positions. $\Delta f_{ad}^{\text{Fres}}$ is the calculated Doppler shift with the Fresnel approximation. According to Fig. 3, there is a residual Doppler-variant Doppler shift Δf_{resi} between Δf_{ad} and $\Delta f_{ad}^{\text{Fres}}$, and the residual shift is indicated by a purple line with bidirectional arrows. Thus, the residual Doppler-variant Doppler shift caused by the Fresnel approximation cannot be ignored during the SPE combination.

III. Autofocusing Algorithm

In Section II, we analyzed the effects of the Fresnel approximation on the SPE estimation and the SPE combination for airborne SAR autofocusing. The effects directly decrease the estimation accuracy of the full-aperture phase error and decrease the resolution of the SAR image. In this section, the SR-PGA method is proposed to eliminate the effect of the Fresnel approximation on the SPE estimation and improve the estimation accuracy. The method employs the hyperbolic model and reconstructs a precise deramping function to compensate for the residual signal phase in the SA. Then, to solve the residual Doppler-variant shift caused by the Fresnel approximation during the SPE combination, the SIR method based on the hyperbolic model is proposed. According to the developed subimage resample in the method, the residual Doppler-variant shift of the adjacent subimages is directly eliminated. Thus, the method can precisely estimate the linear phase error in each SA, further combining multiple SPEs into the high-order full-aperture motion error. Compared with the traditional autofocusing algorithm, the proposed autofocusing method is more suitable for long synthetic aperture autofocusing.

Finally, the method flowchart is shown in Fig. 4, and the detailed processing for the proposed autofocusing algorithm is introduced next.

A. SR-PGA Method

To eliminate the residual signal phase caused by the Fresnel approximation and improve the precision of the SPE estimation, the SR-PGA method is proposed. According to (9), if the phase of the higher order terms of the SA signal is compensated for and the SA signal is transformed into the range-Doppler domain, the peak response's position $\hat{f}_n$ of point target P in the nth SA image in the range-Doppler domain is

$$\hat{f}_n = \frac{2}{\lambda}\eta_1\left(\Delta\hat{t}_n, R_b\right) - \frac{b_n}{2\pi}. \tag{19}$$

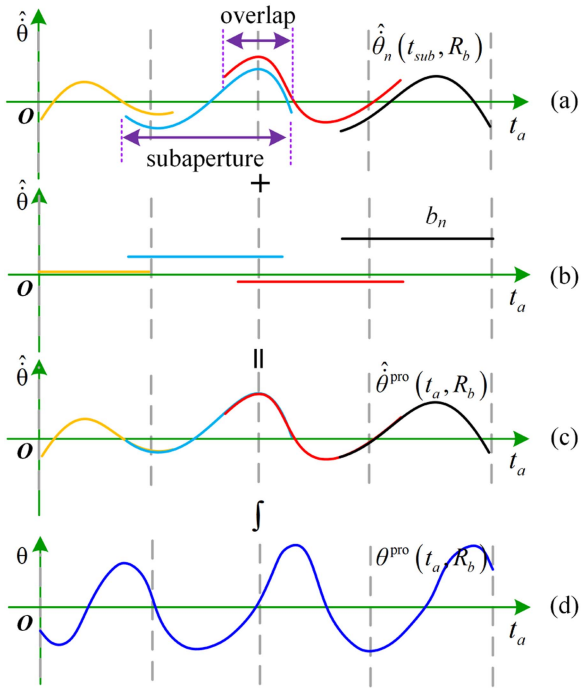

Fig. 7. Schematic diagram of the SPE combination. (a) Obtained SPE gradients. (b) Estimated Doppler shifts. (c) Combined full-aperture phase error gradient. (d) Full-aperture phase error.

TABLE II
SUBAPERTURE IMAGE QUALITY EVALUATION RESULTS

Items	IRW (m)		PSLR (dB)		ISLR (dB)	
	Range	Azimuth	Range	Azimuth	Range	Azimuth
PGA	0.1221	2.0358	-12.32	-10.82	-10.21	-8.95
SR-PGA	0.1219	2.0351	-12.80	-13.03	-10.36	-9.39

The azimuth time spacing $\Delta\hat{t}_n$ can be calculated as

$$\Delta\hat{t}_n = -\frac{R_b}{v}\frac{\left(\left(\hat{f}_n + \frac{b_n}{2\pi}\right)\Big/ f_{am}\right)}{\sqrt{1-\left(\left(\hat{f}_n + \frac{b_n}{2\pi}\right)\Big/ f_{am}\right)^2}} \tag{20}$$

where $f_{am} = 2v/\lambda$. Then, the signal phase of P in the nth SA reconstructed by the estimated $\Delta\hat{t}_n$ in the azimuth time domain is

$$s'\left(t_{\text{sub}}, R_b\right) = \exp\left(-j\frac{4\pi}{\lambda}\sqrt{R_b^2 + \left(v\left(\Delta\hat{t}_n + t_{\text{sub}}\right)\right)^2}\right). \tag{21}$$

According to (6), the constant and first-order terms in (21) are eliminated and the higher order terms of the SA signal phase in the azimuth time domain are reconstructed as

$$s'_{de}\left(t_{\text{sub}}, R_b\right) = \exp\left(\begin{array}{l} -j\frac{4\pi}{\lambda}\sqrt{R_b^2 + \left(v\left(\Delta\hat{t}_n + t_{\text{sub}}\right)\right)^2} \\ +j\frac{4\pi}{\lambda}\sum_{i=0}^{1}\eta_i\left(\Delta\hat{t}_n, R_b\right)\cdot t_{\text{sub}}^i \end{array}\right). \tag{22}$$

Here, we call (22) the precise deramping function to distinguish it from the coarse deramping function in (11). Compared with (11), (22) reconstruct the signal phase with a precise hyperbolic model and eliminate the residual signal phase history of the SA in the 2-D time domain.

TABLE III
IMAGE QUALITY EVALUATION RESULTS

Items	IRW (m)		PSLR (dB)		ISLR (dB)	
	Range	Azimuth	Range	Azimuth	Range	Azimuth
Initial MOCO	0.1652	0.6688	-5.08	-0.22	-1.62	-7.64
PGA-MD	0.1347	0.2328	-3.40	-0.32	-2.99	-1.28
SRPG A-SIR	0.1235	0.1110	-10.09	-13.32	-9.15	-9.40

Multiplying (22) by (9) to match the SA signal phase in the azimuth time domain, one obtains the SA signal after the precise deramping

$$\begin{aligned} s'_n\left(t_{\text{sub}}, R_b\right) &= \exp\left(-j\left(\tfrac{4\pi}{\lambda}\eta_0\left(\Delta\hat{t}_n, R_b\right) - a_n\right)\right) \\ &\times \exp\left(-j2\pi\left(\tfrac{2}{\lambda}\eta_1\left(\Delta\hat{t}_n, R_b\right) - \tfrac{b_n}{2\pi}\right)t_{\text{sub}} + j\theta_n\left(t_{\text{sub}}, R_b\right)\right). \end{aligned} \tag{23}$$

Thus, the azimuth-variant higher order terms of the SA signal phase are matched precisely. Also, (23) only has the SPE that a conventional PGA algorithm can estimate. With the PGA approach [21], the proposed SR-PGA method consists of the following six steps.

Coarse Deramping: The first step is to multiply the coarse deramping function (11) by (9). The product can match the SA signal phase uniformly. An FT in the azimuth dimension is applied to the SA signal after the deramping, and the coarse-focused SA image is obtained in the range-Doppler domain.

Precise Deramping: By adequately selecting strong scatterers in the coarse-focused SA image, one obtains the frequency shift $\hat{f}_n$ of each scatterer and substitutes all $\hat{f}_n s$ into the precise deramping function (22). Then, one multiplies (22) by (9) to match the SA signal phase accurately. After that, an azimuth FT is applied to the processed SA signal, and the SA image after the precise deramping is obtained in the range-Doppler domain.

Circular Shifting: Selecting strong scatterers in the SA image and circularly shifting them to the position with zero Doppler frequency in the Doppler domain can remove the frequency shift caused by the linear term in (9). The circular shifting operation aligns the scatterers, subsequently improving the signal-to-noise ratio for the SPE estimation. The shifting can align regions with a low contrast ratio as well.

Windowing: Windowing can achieve the desired effect of preserving the width of the dominant blur of selected scatterers and discarding scatterers' data that do not contribute to the SPE estimation. With the assumption that the phase error is azimuth-invariant, the strong scatterers in the same SA image have an identical phase error $\theta_n(t_{\text{sub}}, R_b)$. Then, the scatterers are of an exact blurring function. We sum all the spreading functions to obtain a one-dimensional function in the Doppler domain whose width adequately captures the point spread function character and then use an energy threshold to determine the window size. The size decreases for subsequent iterations because the focus level of the SA image increases after each iteration.

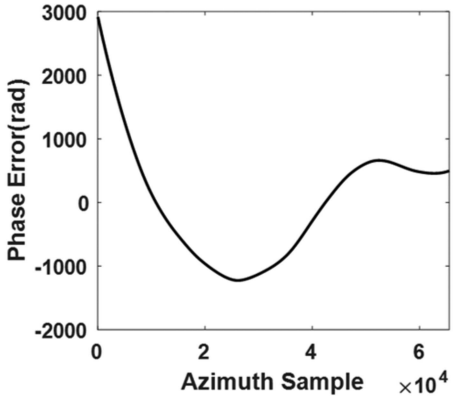

Fig. 8. Estimated motion errors used for the initial MOCO.

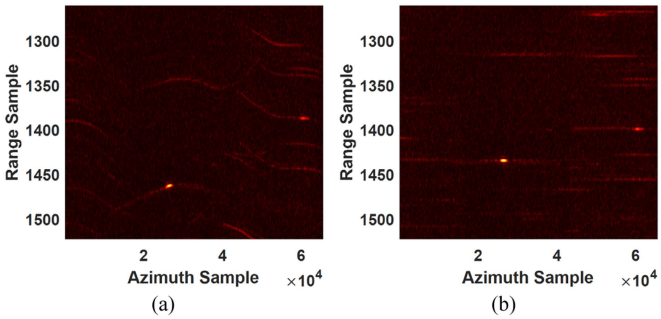

Fig. 9. Range profiles (a) before and (b) after the initial MOCO.

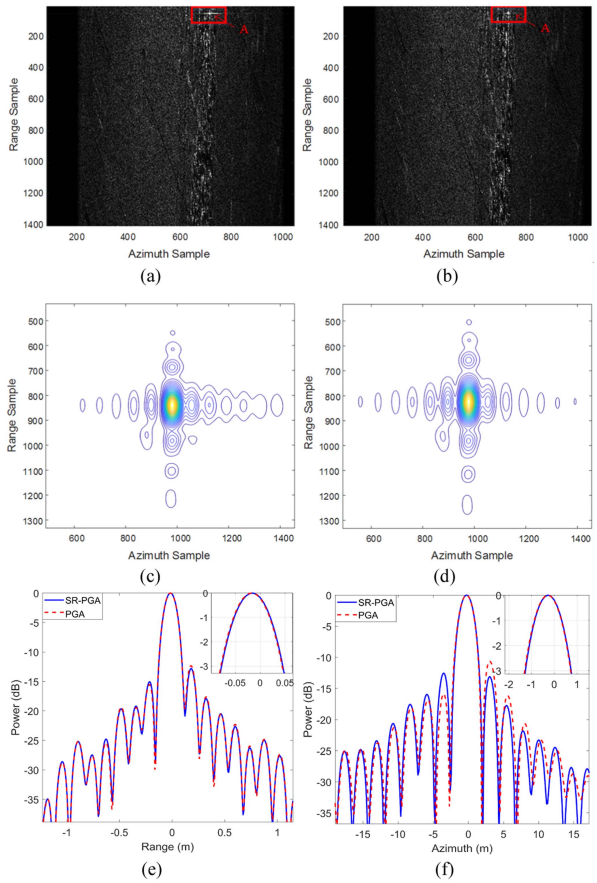

Fig. 10. (a) SA image after the MOCO with SPE obtained by the PGA algorithm. (b) SA image after the MOCO with SPE obtained by the SR-PGA algorithm. (c) Contour map of target A in (a). (d) Contour map of target A in (b). Impulse response curves of target A obtained by the PGA and SR-PGA algorithms. (e) Range profiles. (f) Azimuth profiles.

Phase Gradient Estimation: The shifted and windowed SA image is denoted as $E(f_a, R_b)$, and the inverse FT of $E(f_a, R_b)$ is $\exp(j\theta_n(t_{\text{sub}}, R_b))$. The phase gradient estimation of the nth SA image is given by

$$\hat{\dot{\theta}}_n\left(t_{\text{sub}}, R_b\right) = \sum_{i=1}^{k} \dot{\theta}_{n,i}\left(t_{\text{sub}}, R_b\right) \theta_{n,i}^{*}\left(t_{\text{sub}}, R_b\right) \tag{24}$$

where k is the number of strong point scatterers in the nth SA image. $\dot{\theta}_n(t_{\text{sub}}, R_b)$ denotes the next azimuth time of $\theta_n(t_{\text{sub}}, R_b)$ and $\theta_n^*(t_{\text{sub}}, R_b)$ is the conjugation of $\theta_n(t_{\text{sub}}, R_b)$. The phase gradient $\hat{\dot{\theta}}_n(t_{\text{sub}}, R_b)$ is integrated to obtain the SPE.

Iterative Phase Correction: With an estimated SPE, the phase error is compensated for in the SA data in the azimuth-time domain. The estimation and compensation process is iterative. As the focus of the SA image improves, the spreading functions of individual scatterers become more compact. Once the removal of the Doppler shifts through, the circular shifting reaches the desired accuracy, the iteration stops.

B. Doppler Shift Estimation Based on Doppler Subimage Resampling Method

As discussed in Section II-C, the Fresnel approximation causes a residual Doppler-variant shift in the estimation of b_n. The SIR method is proposed to eliminate the Doppler-variant shift. After the SPE estimated by the SR-PGA method is compensated for the SA data, the data are processed using the coarse deramping function (11). A focused subimage can be obtained in the range-Doppler domain.

Considering P, one takes the nth subimage in the range-Doppler domain as a reference subimage and considers there is no linear term of the SPE in it. According to the second term of (10) and (7b), the relation between the peak response's position f_n of P in the nth subimage and Δt_n is

$$f_n = \frac{2v^2 \Delta t_n}{\lambda \sqrt{R_b^2 + \left(v \Delta t_n\right)^2}}. \tag{25}$$

Since each f_n corresponds to an azimuth time interval Δt_n, the azimuth time interval and the azimuth Doppler frequency in the subimage can be calculated from each other. Then, the focus position f_m of P in the mth subimage is

$$f_m = \frac{2v^2 \left(\Delta t_n + (m-n)\,\Delta T\right)}{\lambda \sqrt{R_b^2 + \left(v\left(\Delta t_n + (m-n)\,\Delta T\right)\right)^2}}. \tag{26}$$

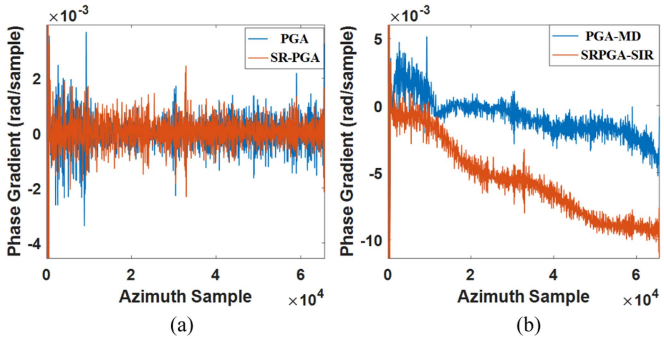

Fig. 11. Phase error gradient in the stripmap data. (a) SPE gradients extracted by the PGA and SR-PGA algorithms. (b) SPE gradients combined by the PGA-MD and SRPGA-SIR algorithms.

Thus, the resampling relationship of f_n and f_m is established as

$$f_m = \frac{2v^2\left(-\frac{R_b}{v}\frac{(f_n/f_{am})}{\sqrt{1-(f_n/f_{am})^2}}+(m-n)\,\Delta T\right)}{\lambda\sqrt{R_b^2+\left(v\left(-\frac{R_b}{v}\frac{(f_n/f_{am})}{\sqrt{1-(f_n/f_{am})^2}}+(m-n)\,\Delta T\right)\right)^2}}. \tag{27}$$

The focus positions in the *n*th and the *m*th subimages of *P* can be aligned by the subimage resampling relationship (27) in the range-Doppler domain, and the Doppler-variant shift is corrected. Here, we assume that the expression of the *n*th subimage of *P* in the range-Doppler domain is $S_n^{\text{img}}(f_a - f_n)$ and the expression of the *m*th subimage of *P* without the liner term b_m of the SPE is $S_m^{\text{img}}(f_a - f_m)$. According to (27), the *n*th subimage of *P* can be resampled into the *m*th subimage to achieve the alignment of the adjacent SA images or

$$S_n^{\text{img}}(f_a - f_n) \overset{(27)}{\rightarrow} S_m^{\text{img}}(f_a - f_m). \tag{28}$$

When the liner phase error exists in the *m*th subimage, the expression of the *m*th subimage of *P* is $S_m^{\text{img}}(f_a - f_m + \frac{b_m}{2\pi})$. The Doppler shift $\frac{b_m}{2\pi}$ can be estimated via cross-correlating $S_m^{\text{img}}(f_a - f_m + \frac{b_m}{2\pi})$ and $S_m^{\text{img}}(f_a - f_m)$ obtained by the resampling of $S_n^{\text{img}}(f_a - f_n)$.

To show the performance of the proposed SIR method, we carried out another simulation with the parameters in Table I. For simplicity, a line signal consisting of eight-point targets was simulated, and there was no phase error in the signal. The time-frequency diagram of the targets' signals is shown in Fig. 5. Two SAs shown in red and blue frames were selected. After coarse deramping, the refocused red and blue subimages were obtained in the range-Doppler domain, and they are called $S_n^{\text{img}}(f_a - f_n)$ and $S_m^{\text{img}}(f_a - f_m)$, respectively. After eliminating the inherent shift between the images, the aligned results of the SA images based on the Fresnel approximation and the proposed SIR method are as shown in Fig. 6. In Fig. 6(a), $S_n^{\text{img}}(f_a - f_n)$ and $S_m^{\text{img}}(f_a - f_m)$ are aligned by eliminating the Doppler-variant shift $\Delta f_{ad}^{\text{Fres}}$ based on the Fresnel approximation. A noticeable shift exists in the magnified box. The estimated Doppler shift is biased. In comparison, the red image $S_n^{\text{img}}(f_a - f_n)$ in Fig. 6(b) is resampled into the blue image $S_m^{\text{img}}(f_a - f_m)$ using the proposed method. There is no Doppler shift, and the bias is eliminated.

After cross-correlating all subimages, the LS technique can be used to obtain the successive Doppler shifts. (The detailed LS technique can be found in [30]). The results are denoted as

$$\mathbf{b}=[b_1 \quad b_2 \quad \cdots b_n \cdots \quad b_N \ ]_{1\times N}. \tag{29}$$

The combined SPE gradients with b_n subtracted by the proposed method is

$$\hat{\dot{\theta}}_n^{\text{pro}}(t_{\text{sub}}, R_b) = \hat{\dot{\theta}}_n(t_{\text{sub}}, R_b) - b_n, 1 \le n \le N. \tag{30}$$

Then, we obtain the combined full-aperture phase error gradient $\hat{\dot{\theta}}^{\text{pro}}(t_a, R_b)$, and integrate it to get the full-aperture phase error $\theta^{\text{pro}}(t_a, R_b)$ in the azimuth time domain. The schematic diagram of the SPE combination is shown in Fig. 7. Fig. 7(a) shows the obtained SPE gradients. The Doppler shifts estimated by cross-correlating all subimages are presented in Fig. 7(b). Adding the SPE gradients and Doppler shifts yields the combined full-aperture phase error gradient shown in Fig. 7(c), and we can get the full-aperture phase error in Fig. 7(d).

IV. Results

To validate the proposed algorithm, we analyze the high-resolution airborne data acquired in a stripmap mode. The SAR system parameters are given in Table I. The coherent processing interval of the raw data was about 32 s, and an aircraft flew at 110 m/s. The motion error estimated by the INS/GPS data is shown in Fig. 8, ranging from about –1000 to 3000 rad for the entire integration time.

Then, the initial MOCO was applied to the raw data. After the RCMC and range compression for the compensated data, 3072 range cells in the range dimension of the data were analyzed. The profiles of the data before and after the initial MOCO are shown in Fig. 9. The phase errors [see Fig. 8] are large enough to cause the profiles to exceed one cell range, as shown in Fig. 9(a). The initial MOCO adequately contains the range error within about one range cell [see Fig. 9(b)]. Thus, after the initial MOCO, one can ignore the influence of range error on the SPE estimation. However, it should be emphasized that the phase errors are still sufficient to defocus the image, and the full-aperture phase error should be estimated further to obtain the refocused image.

In estimating the full-aperture phase error, an overlapping SA strategy was employed. The size of each SA was 1024 samples with the overlapped samples of 512. An SA image in the range-Doppler domain was selected to compare the accuracy of the PGA and SR-PGA algorithms in error estimations. Subimages after compensation of the SPE obtained by the PGA and SR-PGA methods are shown in Fig. 10. Both images are well-focused overall. Fig. 10(a) has an entropy value of 12.1743, whereas the entropy value of Fig. 10(b) is 12.1455. Meanwhile, the same strong scatterer with the red rectangles in Fig. 10(a) and (b) was selected to show its contour maps. The results are illustrated in Fig. 10(c) and (d), respectively. The contour lines are more symmetric after the SR-PGA method than

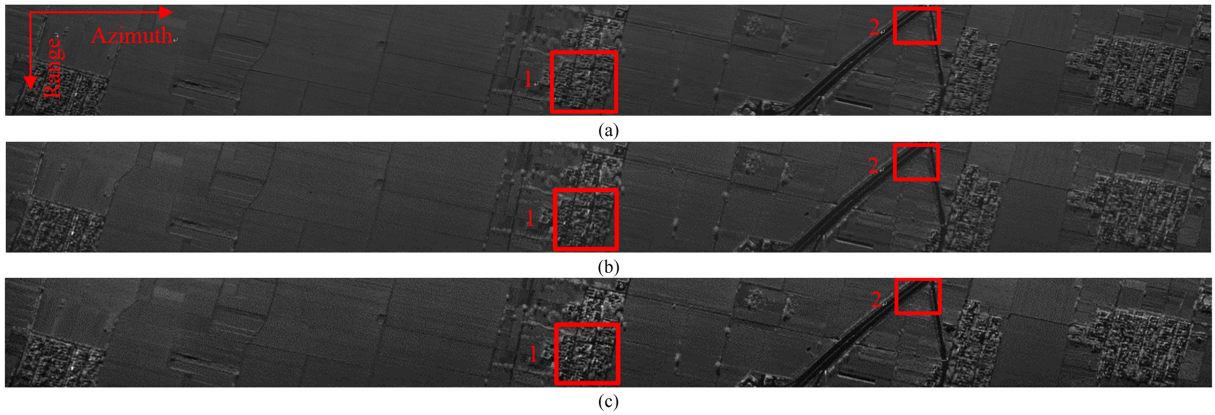

Fig. 12. *X*-band SAR images after the (a) initial MoCo, (b) PGA-MD, and (c) SRPGA-SIR algorithms. The image is about 3520 m in the azimuth and 300 m in the range direction.

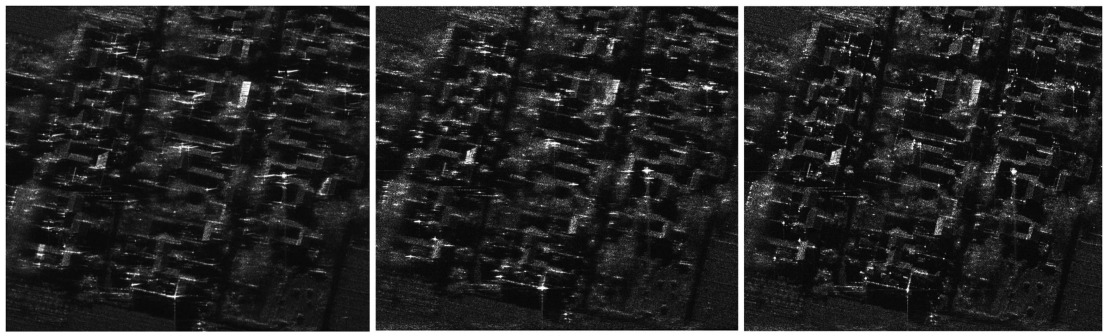

Fig. 13. Close-up views of area 1 in Fig. 12 after the (a) initial MoCo, (b) PGA-MD, and (c) SRPGA-SIR algorithms.

the PGA method. Moreover, to evaluate the focusing results of the scatterer obtained by the SR-PGA and PGA methods, the quantitative results, including the impulse response width (IRW), peak side lobe ratio (PSLR), and integrated side lobe ratio (ISLR) of the scatter, are listed in Table II. The resolution is evaluated by the 3-dB bandwidth of the major lobe. According to the impulse response curves of strong scatter in Fig. 10(f), the azimuth resolutions of both methods are 2.0351 and 2.0358 m, respectively. Because the synthetic aperture time for the SA is short, the azimuth resolution of the scatterer is low. Note that, although the azimuth resolutions obtained by both methods are similar, there is a high-order residual phase error in the PGA and it causes the sidelobes to be not symmetric. Thus, the subimage quality after the SR-PGA method is better than that after the PGA method.

For the sake of description, the traditional autofocusing methods based on the Fresnel approximation are called the PGA-MD method in this article, and the proposed method is named the SRPGA-SIR method. The full-aperture phase errors are obtained by the PGA-MD method and the SRPGA-SIR method, respectively. Fig. 11(a) shows the SPE gradients obtained by the PGA and SR-PGA methods in all SAs, and the gradients differ. The SPE gradients after the PGA-MD and the proposed methods are shown in Fig. 11(b). As the number of azimuth samples increases, the deviation in evaluating the Doppler shift increases and the variation leads to different phase error estimations in a full aperture.

After using the full-aperture phase errors to compensate for the raw data and completing the RCMC, the focused image after the PGA-MD algorithm is shown in Fig. 12(b) and the image after the SRPGA-SIR algorithm in Fig. 12(c). Meanwhile, the focused image after the initial MOCO is shown in Fig. 12(a). Each image is about 3520 m in the azimuth and 300 m in the range. Both are well-focused generally. The close-up views of area 1 and area 2 [see Fig. 12] are shown in Figs. 13 and 14, respectively. Fig. 13(a) is the close-up of area 1 in Fig. 12(a), Fig. 13(b) area 1 in Fig. 12(b), and Fig. 13(c) area 1 in Fig. 12(c). Fig. 14(a) is the close-up of area 2 in Fig. 12(a), Fig. 14(b) area 2 in Fig. 12(b), and Fig. 14(c) area 2 in Fig. 12(c). Buildings and open spaces with scattered trees are better delineated in Fig. 13(c) than in Fig. 13(a) and (b), and the street lamps are better well-focused in Fig. 14(c) than in Fig. 14(a) and (b). Fig. 13(c) is quantitatively better focused than Fig. 13(a) and (b). The image obtained by the initial MOCO is defocusing, which is caused by the lack of precision of the measurement data. Therefore, the full-aperture phase error obtained by the proposed SRPGA-SIR method is more precise than that obtained by the initial MOCO and PGA-MD methods.

Fig. 14. Close-up views of area 2 in Fig. 12 after the (a) initial MoCo, (b) PGA-MD, and (c) SRPGA-SIR algorithms.

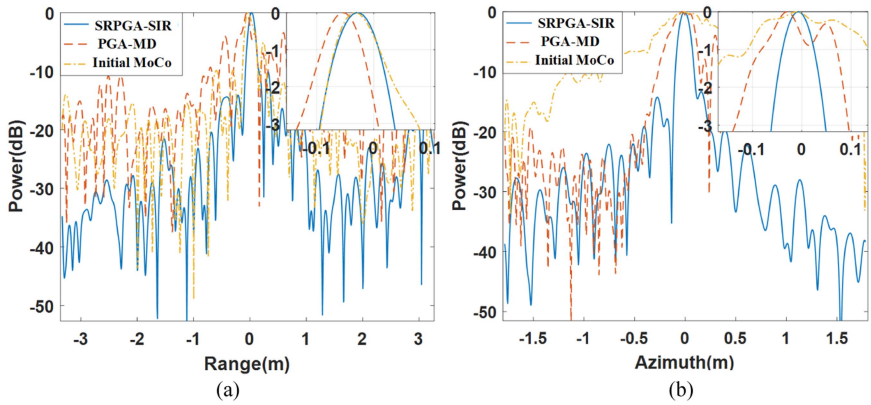

Fig. 15. Impulse response curve comparison of the street lamp 3 in Fig. 14. (a) Range profile. (b) Azimuth profile.

To illustrate the azimuth resolution after the initial MOCO, the PGA-MD and SRPGA-SIR algorithms, we identified a street lamp within area 3 [see Fig. 14], and the street lamp can be seen as a strong scatter. The quantitative results, including the IRW, PSLR, and ISLR of the strong scatter, are listed in Table III. The resolution is evaluated by the 3-dB bandwidth of the major lobe. According to the impulse response curves of strong scatter in Fig. 15, the 2-D spatial resolution is 0.1235 m $\times$ 0.1110 m (range $\times$ azimuth). Furthermore, one can argue that the SRPGA-SIR algorithm could output an image with a high azimuth resolution.

V. Discussion

A. Analysis of Influence of Subaperture Number

Generally, the more the number of the SAs is, the more serious the accumulation of phase errors is. There are two reasons for the accumulation of phase errors. The first reason is that the accuracy of the SPE estimation may not be high, and even the estimated SPE is wrong. The second one is the shift estimation of the adjacent SPEs, which depends on the accuracy of the estimated SPE. In the proposed algorithm, there are two aspects of improvement are proposed to minimize the influence of the number of SAs and avoid the accumulation of phase errors as soon as possible. The SR-PGA method is proposed to improve the accuracy of the estimated SPE, and the SIR method is used to improve the accuracy of the estimated Doppler shift of the adjacent SA images.

B. Applicability of Proposed Algorithm

To ensure well-focused results in the azimuth dimension, the phase error must be within $\pm\pi/4$. As plotted in Fig. 2, the residual azimuth-variant signal phase $\phi_{\text{resi}}(t_{\text{sub}}, R_b)$ in an SA increases as $|\Delta t_n|$ increases. Thus, to obtain a well-focused image, the range resolution ρ_r should meet

$$\max\left(\phi_{\text{resi}}\left(t_{\text{sub}}, R_b\right)\right) * \frac{R_b\lambda}{2\rho_r v T_{\text{sub}}} \leq \frac{\pi}{4} \tag{31a}$$

$$\text{or } \max\left(\phi_{\text{resi}}\left(t_{\text{sub}}, R_b\right)\right) * \frac{2R_b\lambda}{\pi v T_{\text{sub}}} \leq \rho_r \tag{31b}$$

where the SA azimuth duration $T_{\text{sub}} = n_a^{SA}/PRF$. When $\phi_{\text{resi}}(t_{\text{sub}}, R_b)$ and ρ_r do not meet the aforementioned relationship, the proposed algorithm should be applied.

Future work includes extending this proposed algorithm to combine with the 2-D image autofocusing methods for obtaining the ultrahigh-resolution SAR image, in which the proposed algorithm can estimate and compensate for the spatial-invariant motion errors and the 2-D autofocusing methods can compensate for the 2-D spatial-variant motion errors, which exist in range

and azimuth dimensions. After that, a well-focused SAR image can be obtained.

VI. Conclusion

In this article, high-resolution airborne SAR autofocusing with a precise hyperbolic model is studied. In terms of the SPE estimation, the SR-PGA method is proposed, in which the precise deramping based on the hyperbolic model is reconstructed to eliminate the residual signal phase and improve the estimation accuracy of the SPE. In addition, an SIR method based on the hyperbolic model is proposed to eliminate the residual Doppler-variant shift between the adjacent subimages and further improve the accuracy of the SPE combination. The proposed algorithm is effective as shown in simulations and analyses of acquired raw airborne SAR datasets. It is a viable option to form well-focused high-resolution images.

References

[1] A. Moreira, P. Prats-Iraola, M. Younis, G. Krieger, I. Hajnsek, and K. P. Papathanassiou, "A tutorial on synthetic aperture radar," *IEEE Geosci. Remote Sens. Mag.*, vol. 1, no. 1, pp. 6–43, Mar. 2013.

[2] M. Xing, X. Jiang, R. Wu, F. Zhou, and Z. Bao, "Motion compensation for UAV SAR based on raw radar data," *IEEE Trans. Geosci. Remote Sens.*, vol. 47, no. 8, pp. 2870–2883, Aug. 2009.

[3] J. Chen, B. Liang, J. Zhang, D.-G. Yang, Y. Deng, and M. Xing, "Efficiency and robustness improvement of airborne SAR motion compensation with high resolution and wide swath," *IEEE Geosci. Remote Sens. Lett.*, vol. 19, 2022, Art. no. 4004005.

[4] J. Chen, J. Zhang, Y. Jin, H. Yu, B. Liang, and D.-G. Yang, "Real-time processing of spaceborne SAR data with nonlinear trajectory based on variable PRF," *IEEE Trans. Geosci. Remote Sens.*, vol. 60, 2022, Art. no. 5205212.

[5] X. Chen, G.-C. Sun, M. Xing, B. Li, J. Yang, and Z. Bao, "Ground Cartesian back-projection algorithm for high squint diving TOPS SAR imaging," *IEEE Trans. Geosci. Remote Sens.*, vol. 59, no. 7, pp. 5812–5827, Jul. 2021.

[6] J. Chen, M. Xing, H. Yu, B. Liang, J. Peng, and G.-C. Sun, "Motion compensation/autofocus in airborne synthetic aperture radar: A review," *IEEE Geosci. Remote Sens. Mag.*, vol. 10, no. 1, pp. 185–206, Mar. 2022.

[7] H. Cantalloube and P. Dubois-Fernandez, "Airborne X-band SAR imaging with 10 cm resolution: Technical challenge and preliminary results," *IEE Proc. Part F, Radar, Sonar Navigation*, vol. 153, no. 2, pp. 163–176, 2006.

[8] L. Zhang, J. Sheng, M. Xing, Z. Qiao, T. Xiong, and Z. Bao, "Wavenumber-domain autofocusing for highly squinted UAV SAR imagery," *IEEE Sensors J.*, vol. 12, no. 5, pp. 1574–1588, May 2012.

[9] L. Zhang, Z. Qiao, M.-D. Xing, L. Yang, and Z. Bao, "A robust motion compensation approach for UAV SAR imagery," *IEEE Trans. Geosci. Remote Sens.*, vol. 50, no. 8, pp. 3202–3218, Aug. 2012.

[10] K. A. C. De Macedo, R. Scheiber, and A. Moreira, "An autofocus approach for residual motion errors with application to airborne repeat-pass SAR interferometry," *IEEE Trans. Geosci. Remote Sens.*, vol. 46, no. 10, pp. 3151–3162, Oct. 2008.

[11] H. Lin, J. Chen, M. Xing, X. Chen, D. You, and G. Sun, "2-D frequency autofocus for squint spotlight SAR imaging with extended omega-K," *IEEE Trans. Geosci. Remote Sens.*, vol. 60, 2022, Art. no. 5211312.

[12] X. Mao, X. He, and D. Li, "Knowledge-aided 2-D autofocus for spotlight SAR range migration algorithm imagery," *IEEE Trans. Geosci. Remote Sens.*, vol. 56, no. 9, pp. 5458–5470, Sep. 2018.

[13] C. Jianlai and Y. Hanwen, "Wide-beam SAR autofocus based on blind RS," *Sci. China Inf. Sci.*, pp. 1674–733X, 2022.

[14] W. Xu, B. Wang, M. Xiang, R. Li, and W. Li, "Image defocus in an airborne UWB VHR microwave photonic SAR: Analysis and compensation," *IEEE Trans. Geosci. Remote Sens.*, vol. 60, 2022, Art. no. 5213518.

[15] L. Yang et al., "Integration of rotation estimation and high-order compensation for ultrahigh-resolution microwave photonic ISAR imagery," *IEEE Trans. Geosci. Remote Sens.*, vol. 59, no. 3, pp. 2095–2115, Mar. 2021.

[16] N. Li et al., "MOCO for high-resolution ScanSAR via full-aperture processing," *IEEE J. Sel. Topics Appl. Earth Observ. Remote Sens.*, vol. 8, no. 4, pp. 1721–1726, Apr. 2015.

[17] G. Xu, M. Xing, L. Zhang, and Z. Bao, "Robust autofocusing approach for highly squinted SAR imagery using the extended wavenumber algorithm," *IEEE Trans. Geosci. Remote Sens.*, vol. 51, no. 10, pp. 5031–5046, Oct. 2013.

[18] Z. Ding et al., "An autofocus approach for UAV-based ultrawideband ultrawidebeam SAR data with frequency-dependent and 2-D space-variant motion errors," *IEEE Trans. Geosci. Remote Sens.*, vol. 60, 2022, Art. no. 5203518.

[19] T. M. Calloway and G. W. Donohoe, "Subaperture autofocus for synthetic aperture radar," *IEEE Trans. Aerosp. Electron. Syst.*, vol. 30, no. 2, pp. 617–621, Apr. 1994.

[20] J. Chen, M. Xing, G.-C. Sun, and Z. Li, "A 2-D space-variant motion estimation and compensation method for ultrahigh-resolution airborne stepped-frequency SAR with long integration time," *IEEE Trans. Geosci. Remote Sens.*, vol. 55, no. 11, pp. 6390–6401, Nov. 2017.

[21] D. E. Wahl, P. H. Eichel, D. C. Ghiglia, and C. V. Jakowatz, "Phase gradient autofocus-a robust tool for high resolution SAR phase correction," *IEEE Trans. Aerosp. Electron. Syst.*, vol. 30, no. 3, pp. 827–835, Jul. 1994.

[22] H. L. Chan and T. S. Yeo, "Noniterative quality phase-gradient autofocus (QPGA) algorithm for spotlight SAR imagery," *IEEE Trans. Geosci. Remote Sens.*, vol. 36, no. 5, pp. 1531–1539, Sep. 1998.

[23] Y. Liu et al., "High-resolution real-time imaging processing for spaceborne spotlight SAR with curved orbit via subaperture coherent superposition in image domain," *IEEE J. Sel. Topics Appl. Earth Observ. Remote Sens.*, vol. 15, pp. 1992–2003, 2022.

[24] Y. Hai et al., "Microwave photonic SAR high-precision imaging based on optimal subaperture division," *IEEE Trans. Geosci. Remote Sens.*, vol. 60, 2022, Art. no. 5232317.

[25] S.-S. Yan et al., "Along-track motion compensation approach for airborne wide-beam SAR based on sub-aperture processing," *Electron. Lett.*, vol. 48, no. 8, 2012, Art. no. 1.

[26] P. Prats, A. Reigber, and J. J. Mallorqui, "Topography-dependent motion compensation for repeat-pass interferometric SAR systems," *IEEE Geosci. Remote Sens. Lett.*, vol. 2, no. 2, pp. 206–210, Apr. 2005.

[27] A. Potsis et al., "Sub-aperture algorithm for motion compensation improvement in wide-beam SAR data processing," *Electron. Lett.*, vol. 37, no. 23, 2001, Art. no. 1.

[28] O. O. Bezvesilniy, I. M. Gorovyi, and D. M. Vavriv, "Estimation of phase errors in SAR data by local-quadratic map-drift autofocus," in *Proc. 13th Int. Radar Symp.*, 2012, pp. 376–381.

[29] D. G. Thompson, J. S. Bates, and D. V. Arnold, "Extending the phase gradient autofocus algorithm for low-altitude stripmap mode SAR," in *Proc. IEEE Radar Conf. Radar Next Millennium*, 1999, pp. 36–40.

[30] D. Zhu, R. Jiang, X. Mao, and Z. Zhu, "Multi-subaperture PGA for SAR autofocusing," *IEEE Trans. Aerosp. Electron. Syst.*, vol. 49, no. 1, pp. 468–488, Jan. 2013.

[31] R. Bamler, "A comparison of range-Doppler and wavenumber domain SAR focusing algorithms," *IEEE Trans. Geosci. Remote Sens.*, vol. 30, no. 4, pp. 706–713, Jul. 1992.

Yuhui Deng (Graduate Student Member, IEEE) was born in Cangzhou, China, in 1994. He received the B.S. degree in communications engineering from the Xi'an University of Posts and Telecommunications, Xi'an, China, in 2018. He is currently working toward the Ph.D. degree in signal processing with the National Laboratory of Radar Signal Processing, Xidian University, Xi'an, China.

His research interests include synthetic aperture radar (SAR) imaging and SAR motion compensation.

Hui Wang (Senior Member, IEEE) was born in Harbin, China, in 1972. She received the Ph.D. degree in communication and information system from the Harbin Institute of Technology, Harbin, China, in 2009.

She was engaged in research on advanced technologies related to synthetic aperture radar for a long time. She is a well-known expert in the field of SAR and a pioneer in the field of spaceborne millimeter-wave SAR in China. She is currently the Chief Technical Director with the Shanghai Academy of Spaceflight Technology, Shanghai, China, in the field of millimeter-wave SAR system, as well as the Director with SAST Millimeter Wave Imaging Laboratory and Shanghai Key Laboratory of Aerospace Millimeter Wave Information Technology, Shanghai, China. She is also the Doctoral Supervisor with the Harbin Institute of Technology and Shanghai Jiao Tong University, Shanghai, China.

Dr. Wang is the Vice Chairperson of the IEEE Geoscience and Remote Sensing Society Shanghai Branch, as well as the editorial board member of Shanghai Aerospace Magazine for part-time jobs.

Guang-Cai Sun (Senior Member, IEEE) received the master's degree in communications engineering from the Xi'an University of Posts and Telecommunications, Xi'an, China, in 2006, and the Ph.D. degree in signal and information processing from Xidian University, Xi'an, China, in 2012.

He is currently a Professor with the National Laboratory of Radar Signal Processing, and also with the Collaborative Innovation Center of Information Sensing and Understanding, Xidian University. He has authored or coauthored one book and more than 50 papers. His research interests include imaging of several SAR modes, moving target detection, and imaging.

Yong Wang (Senior Member, IEEE) received the B.Sc. degree in electrical engineering from the Northwestern Polytechnical University, Xi'an, China, in 1982, and the Ph.D. degree in geography from the University of California, Santa Barbara, Santa Barbara, CA, USA, in 1992, focusing on synthetic aperture radar and its application in forested environments.

He is currently a Full Professor with the School of Resources and Environment, University of Electronic Science and Technology of China, Chengdu, China. His research interests include application of remotely sensed and geospatial datasets to environments.

Dr. Wang is an Associate Editor for the *Remote Sensing of Environment* and IEEE TRANSACTIONS ON GEOSCIENCE AND REMOTE SENSING.

Wenkang Liu (Member, IEEE) was born in Dancheng County, China, in 1994. He received the B.S. degree in electronic information engineering from Xidian University (XDU), Xi'an, China, in 2015, and the Ph.D. degree in signal and information processing from the National Laboratory of Radar Signal Processing, XDU, in 2020, with a focus on the imaging techniques of MEO/GEO SAR.

From 2019 to 2020, he was a visiting student with Naples University of "Parthenope," Naples, Italy. Since 2022, he has been an Associate Professor with the Academy of Advanced Interdisciplinary Research, XDU, where he is responsible for the development of the data processing and calibrating modules for the first GEO SAR to be launched. His research interests include novel space-borne radar system designing, SAR imaging algorithm development, multipass SAR signal processing, and SAR waveform designing.

Jun Yang (Member, IEEE) was born in Hubei, China, in 1984. He received the master's degree in communications engineering from the Post and Telecommunication Institution, Xi'an, China, in 2006, and the Ph.D. degree in signal and information processing from Xidian University, Xi'an, China, in 2014.

He is currently a Lecturer with the College of Geomatics, Xi'an University of Science and Technology, Xi'an, China. His research interests include imaging of several synthetic aperture radar modes, moving target detection, and imaging.

Mengdao Xing (Fellow, IEEE) received the B.S. and Ph.D. degrees in electrical engineering from Xidian University, Xi'an, China, in 1997 and 2002, respectively.

He is currently a Professor with the National Laboratory of Radar Signal Processing, Xidian University. He holds the appointment of the Associate Dean with the Academy of Advanced Interdisciplinary Research, Xidian University. He has authored or coauthored more than 200 refereed scientific journal articles and two books about synthetic aperture radar (SAR) signal processing. His research has been supported by various funding programs, such as National Science Fund for Distinguished Young Scholars. His current research interests include SAR, inversed SAR, sparse signal processing, and microwave remote sensing.

Dr. Xing serves as an Associate Editor for radar remote sensing of the IEEE TRANSACTIONS ON GEOSCIENCE AND REMOTE SENSING. The total citation times of his research are greater than 8000. He was rated as Most Cited Chinese Researchers by Elsevier. He has achieved more than 40 authorized China patents.